

Supporting information for: BSim 2.0: an advanced agent-based cell simulator

Antoni Matyjaszkiewicz,^{†,‡,⊥} Gianfranco Fiore,^{†,‡,⊥} Fabio Annunziata,^{¶,‡} Claire S. Grierson,^{§,‡} Nigel J. Savery,^{¶,‡} Lucia Marucci,^{*,†,‡,⊥,Ⓢ} and Mario di Bernardo^{*,†,‡,||,Ⓢ}

[†]*Department of Engineering Mathematics, University of Bristol, Merchant Venturers' Building, Woodland Road, Bristol BS8 1UB, UK*

[‡]*BrisSynBio, Life Sciences Building, Tyndall Avenue, Bristol BS8 1TQ, UK*

[¶]*School of Biochemistry, University of Bristol, Biomedical Sciences Building, University Walk, Bristol BS8 1TD, UK*

[§]*School of Biological Sciences, University of Bristol, Life Sciences Building, Tyndall Avenue, Bristol BS8 1TQ, UK*

^{||}*Department of Electrical Engineering and Information Technology, University of Naples Federico II, 80125, Naples, Italy*

[⊥]*Co-first authors*

[Ⓢ]*Contributed equally to this work*

E-mail: lucia.marucci@bristol.ac.uk; m.dibernardo@bristol.ac.uk

Contents

1	Online availability	S3
2	Methods and implementation of new features	S3
2.1	Cellular growth mechanics	S3
2.2	Cell-cell interactions	S4
2.3	Simulation domain used in our case study	S6
2.4	Cell-geometry interaction	S6
2.5	Cell position relaxation	S7
2.6	Delay equations for GRNs	S7
3	Validation: a consortium case study	S8
3.1	BSim 2.0 implementation	S9
3.2	Results	S10
3.2.1	Note on selection of single cells	S13
3.2.2	Computational resources	S14
3.3	Implications for microfluidic chemostats	S14
	References	S15
4	SI Figures and Movies	S18
4.1	Supplementary Figures	S18
4.2	Supplementary Movies	S26

1 Online availability

The original version of *BSim* is specified in (S1). *BSim 2.0* and further information regarding details of the structure of a *BSim* simulation, its key features, and implementation details including tutorials for generating all the necessary simulation elements (Figure S1) are available at <https://github.com/bsim-bristol/bsim>. The full source code of *BSim 2.0*, including the code required to run the case study simulations presented here, is available to download at the same URL (<https://github.com/bsim-bristol/bsim>). The *BSim 2.0* source distribution comes packaged with fully commented example scenarios illustrating individually, and in combination, all of the features available to the user (to date there are 25 such scenarios available online).

2 Methods and implementation of new features

In this section we expand in further detail the methods used to implement all of the new features of *BSim 2.0* described in the main text.

2.1 Cellular growth mechanics

All cells are simulated as individual agents with capsular geometry, with individual cell radius r_{cell} . Cell growth (Equation 1) is modelled using a per-cell ordinary differential equation (ODE) model of rod elongation over time as in (S2)

$$\frac{dL}{dt} = k_{\text{growth}} L \left(\frac{1 - L}{L_{\text{max}}} \right), \quad (1)$$

where L is the cell length, k_{growth} is the growth rate and L_{max} is the limiting length (Table S1). At the beginning of simulations, cells were initialised with lengths normally distributed about $L_{\text{init}} = 2.25 \mu\text{m}$ with standard deviation of 10%.

Division occurs once the mother cell has passed a set constant threshold length L_{div} .

Initial cell length for all simulations was set to $2.25 \mu\text{m}$ with a maximal division threshold of $4.5 \mu\text{m}$ (Table S1). When cells were randomly initialised at the start of simulations that included growth, the initial cell lengths for individual cells were chosen according to a Normal distribution centered on $2.25 \mu\text{m}$ with a variance of 10%.

In the cases where cells were deterministically arranged the cell count was varied from a minimum of 10 cells in the smallest domain size investigated, to a maximum count such that the density of cells was effectively maximised for a given domain geometry. Here, cells' positions were seeded at $t = 0$ such that all cells maintained an approximately equal distance between each other, and the boundaries of the simulation domain (further details below: 'static population distributions').

The elongation rate was chosen such that cell division occurred on average after 25 minutes of growth (normal for *E. coli* cells, in log phase, growing in a rich medium as would be the case in a microfluidic chemostat). Upon division, daughter cells' positions and lengths were perturbed by a small amount (randomly chosen, with an amplitude between $\pm 3\%$ of their length) at the location of division in order to break axial symmetry as in (S2).

Table S1: Model parameters for capsular cell morphology, growth and geometric interaction mechanics.

Description	Parameter	Value	Source
Cell radius	r_{cell}	$0.5 \mu\text{m}$	(S2)
Growth rate	k_{growth}	0.002 s^{-1}	20–25min generation time(S3). (S2) (S2) (S2)
Starting length	L_{init}	$2.25 \mu\text{m}$	
Limiting length	L_{max}	$2.5 \times l_{\text{init}} \mu\text{m}$	
Division threshold	L_{div}	$2.0 l_{\text{init}} \mu\text{m}$	
Internal spring constant	k_{int}	50 (units as Equation 2)	Empirically selected.
Cell-cell spring constant	k_{cell}	50 (units as Equation 3)	Empirically selected.
Cell-geometry spring constant	k_{wall}	50 (units as Equation 4)	Empirically selected.

2.2 Cell-cell interactions

Cells are represented by capsular volumes, typical of *E. coli*. Specifically, cells are parametrised by the two end points (designated \mathbf{x}_1 and \mathbf{x}_2) of a line segment along which a sphere of radius r_{cell} is extruded resulting in a capsule-shaped excluded volume. As the cells grow in time

their length increases and thus a constraint on the distance d_L between \mathbf{x}_1 and \mathbf{x}_2 is imposed (we want d_L to tend toward L at all times). In order to maintain this constraint, we define a force of magnitude

$$F_L = \frac{1}{2}k_{\text{int}}(d_L - L)^2, \quad (2)$$

as in (S2), for every cell in the simulation. This force is computed, at each step of the relaxation described below, and applied at \mathbf{x}_1 and \mathbf{x}_2 in the direction along the cell's main axis.

The magnitudes of cell-cell interaction forces $F_{\text{cell}}^{(i,j)}$ for a pair of cells i and j are computed using a semi-rigid-body approach as previously employed in (S2, S4–S6) amongst others. In the absence of individual motility, cells are allowed to grow following the rules specified above. The combined effects of growth, interaction between cells, and interactions with the surrounding geometry mean that at the end of every simulation time-step some combination of cells and the surrounding geometry are intersecting in a non-physical manner. This is resolved by computing, for each pair of intersecting cells, an overlap-dependent volume exclusion force (S7), as originally employed in molecular dynamics simulations and analogously extended to spherical cells (S6) and subsequently capsular cells (S2). For any pair of cells i and j we define the penetration depth, if it exists, as $d_{\text{cell}}^{(i,j)}$. We can then compute this cell-cell interaction force as

$$F_{\text{cell}}^{(i,j)} = -\frac{2}{5}k_{\text{cell}} \sum_{j \in \text{Neighbours}} \left(d_{\text{cell}}^{(i,j)}\right)^{\frac{5}{2}}, \quad (3)$$

once the set of all possible j i.e., the neighbours of cell i has been computed. The computation of a cell's neighbourhood can be either performed as a factorial loop through all cells in the simulation or, more efficiently (Figure S2), by defining a grid over the spatial domain and testing for intersection only between cell i and the cells in neighbouring grid squares; both methods are implemented in *BSim 2.0*.

2.3 Simulation domain used in our case study

The simulation domain (representing a microfluidic chamber, or microchemostat) was represented by a cuboid geometry (Figure S3), with dimensions that were varied between $12 \times 10 \times 1 \mu\text{m}^3$ and $100 \times 85 \times 1 \mu\text{m}^3$ in the x , y , and z axes respectively. The largest simulated chamber was equivalent to those used in *in-vivo* experiments, such as those in (S8, S9).

The chamber was closed on all sides except the bottom (x -aligned) long side. All boundaries were closed to physical cell passage, except for this single open side through which signal diffusion occurred which permitted passage of cells in order to model the removal of cells via external flow as occurs in real microfluidic experiments (for example, those discussed in (S8, S10)). A lateral force corresponding to a typical flow rate of $250 \mu\text{m s}^{-1}$ was then applied to any cells passing outside the open boundary of the domain.

2.4 Cell-geometry interaction

Geometry is represented internally using boxes or triangular-element meshes. Cell-geometry interactions are implemented using a semi rigid-body approach similar to that for cell-cell interactions, with methods defined in (S11, S12).

At each time step, potential intersections between cells and geometry in the domain are computed. In brief, a capsule-plane intersection test is performed for each agent and each mesh element. If a potential collision could occur, the intersection test is refined to take into account the area of the triangular element that may intersect the agent's bounding capsule. Finally, the overlap distance $d_{\text{wall}}^{(i,e)}$ between the plane of an element e and the capsule is computed and an overlap-dependent volume exclusion force magnitude, as for the cell-cell interactions, is computed for any cell that is in contact with an element of the mesh

$$F_{\text{wall}}^{(i,e)} = -\frac{2}{5}k_{\text{wall}} \sum_{e \in \text{Elements}} \left(d_{\text{wall}}^{(i,e)}\right)^{\frac{5}{2}}. \quad (4)$$

Collision force magnitudes are only computed and applied for those elements which are in fact in interpenetration with a capsule; however, multiple elements may exert a repulsive force on a single capsule (e.g., in the case of cells at a concave corner).

2.5 Cell position relaxation

The final step in solving position constraints and resolving unphysical penetration between cell pairs, and cells and geometry involves applying the computed force magnitudes defined in the previous sections to the cells, and integrating the cells' positions. This is referred to as the relaxation step, since after all collision pairs and forces are defined the positions of all cells are simultaneously relaxed according to the computed forces in order to minimise all overlaps of all intersections (S4). The forces are applied in directions which vary according to the type of constraint force:

1. F_L is applied with equal and opposite magnitude to \mathbf{x}_1 and \mathbf{x}_2 along the major axis of the capsule (the vector from \mathbf{x}_1 and \mathbf{x}_2);
2. $F_{\text{cell}}^{(i,j)}$ is applied in the direction between the closest two points on the major axis of the two colliding cells and its application to \mathbf{x}_1 and \mathbf{x}_2 is linearly weighted according to the distance of the intersection point from \mathbf{x}_1 and \mathbf{x}_2 ;
3. $F_{\text{wall}}^{(i,e)}$ is applied along the normal of the element e in the direction of the cell i .

2.6 Delay equations for GRNs

In single-cell models gene regulatory networks (GRNs) are typically simulated using ordinary differential equation (ODE), or delayed differential equation (DDE) systems either to reduce the number of equations in the model or to take into account mechanistic delays affecting the biochemical reactions of interest (S13, S14). In *BSim 2.0* we leverage a unified ODE and DDE solver framework provided by the OpenSourcePhysics¹ library. Available solvers include both

¹<http://www.opensourcephysics.org/>

fixed-step and variable-step solvers of order 2–8. State variables can be coupled to external chemical fields, with an exchange of chemicals occurring once every major simulation time step according to a linear gradient (as is typical in the modelling of small signalling molecule diffusion, e.g., (S15, S16)).

Upon cell division, internal contents are split between the daughter cells. Daughter cells inherit the perturbed (according to their relative volume) current state of all dependent variables (as is typical in agent-based approaches (S17)). New DDE objects are created for the, also newly-instantiated, daughter cells; the mother cell’s DDE system is re-initialised upon division. Since DDEs are being simulated, it is necessary to consider the effects of history upon division. To simplify proceedings, the history for each state variable in an internal system is reset to a constant value equal to that state variable’s value at division time $t = t_{\text{div}}$. This may potentially cause the solution of a system to diverge upon division from a solution that had simply continued with a fully-defined history; thus our method may not be appropriate in all cases, and when modelling cell division coupled to DDEs in this way care should be taken to judiciously deal with differences in time scales between the cell lifetime and the delay lengths. In the specific situation of our case study, we found that the dynamics of the full system (oscillations with period greater than 3 hours) vary on a timescale far longer than the cell cycle (approximately 20–25 min) and significantly longer than the delay employed in the model (7.5 min).

3 Validation: a consortium case study

Here we more extensively describe the system of our case study presented in the main text, and its implementation details in *BSim 2.0*. The system described in (S9) consists of a consortium of engineered cells of two types, Activator and Repressor cells; these are coupled together through two spatially uniform external chemical concentrations. This biological system is ideal for stress-testing our newly implemented features: its desired behaviour de-

depends strongly on functional feedbacks between multiple spatially distributed populations of cells through a diffusive cell-cell quorum sensing mechanism, so that they act together as a consortium, with internal single-cell GRNs characterised by delayed and highly nonlinear dynamics. The growth of cellular populations inside a microfluidic chemostat is significantly affected by both the chemostat topology and the single-cell morphology (S2, S5). In the case of multiple populations such dynamics are of particular interest and must be simulated accurately in order to correctly predict a consortium-wide behaviour particularly when prototyping new circuit designs. Accurate representation of internal GRN dynamics is crucial.

3.1 BSim 2.0 implementation

The original system is modelled by 16 coupled nonlinear DDEs; this includes both the internal dynamics of two engineered species' GRNs, and those of the two external chemicals I and H , whose concentrations have no spatial component in the original model description. Further details of the original model equations can be found in the Supplementary Material of (S9). In our *BSim 2.0* implementation (Figure S3) we first split the original system as follows: equations corresponding to (i) Activator cells' internal dynamics; (ii) Repressor cells' internal dynamics; (iii) external chemical concentrations. Activator and Repressor cells were implemented as capsular cells, with internal GRN dynamics described by coupled DDEs corresponding to the components (i) and (ii) respectively of the split system. The two external chemicals were modelled as spatially non-uniform discretized diffusion PDEs, which were coupled to intracellular GRN dynamics according to each individual cell's position.

In BSim 2.0, the dynamics of both the signalling species I and H are modelled using two partial differential equations (PDEs) — diffusion equations with an added local first order degradation term simulated using a finite volume discretization — with diffusion and degradation rates specified as in (S16). Reflective boundary conditions were applied to the discretized equations for the five closed sides of the domain. A Dirichlet boundary condition was applied at the bottom open side, with a constant zero external concentration representing

the diffusion-dominated flow out of the microfluidic chamber. Unless otherwise specified, the rate of flux at this boundary was set to $0.1 \mu\text{m}^2\text{sec}^{-1}$, corresponding to the value of μ_e , the external dilution, as originally specified in (S9). Internal per-cell GRNs were implemented as two distinct systems of delay equations. The intra-cellular embedded GRN equations were directly coupled to the discretized concentrations of I and H at the position of each cell, which were sampled and exchanged at every time step of the simulation.

3.2 Results

We first investigated the simplest possible scenario, that of a small $12 \times 10 \times 1 \mu\text{m}^3$ chamber with two fixed cells: a single Activator cell and single Repressor cell (Figure S5). We varied the rate of diffusion through the open microchemostat boundary as well as the rate of degradation of the signalling chemicals, in order to ascertain whether the original model's parameters would allow the system to function correctly when implemented as-is into a spatially-extended model. When no flux was applied across the open boundary (Figure S5-a and -b) the model performed correctly, i.e., consortium-wide oscillations equivalent to those generated by the non-agent-based DDE model were measured, regardless of whether spatially uniform degradation was present in the model or not. We then tested the model with an open boundary leak rate equal to the diffusivity of the signalling molecules (Figure S5-c). In this case the model failed to generate robust oscillations across the consortium, since the concentrations of signalling chemicals I and H were decreased too rapidly with respect to the rest of the system thus not allowing the two populations to communicate correctly. A more conservative leak rate, equivalent to the dilution rate specified in (S9), rectified this issue (Figure S5-d).

We then investigated the range of system behaviours as the size of a fully-packed chamber was varied (Figure S6). Here, we chose the hypothetical 'worst-case' experimental scenario where the two populations are distributed as two blocks in opposing halves of the microchemostat (each being uniformly distributed within its own half). We refer to this

scenario as the ‘worst-case’ since the average cell-cell distance (between cells in opposing populations) is maximal here impacting significantly on the efficacy of intercellular signalling which depends on rapid diffusion between populations. In this case, for all chambers larger than the smallest tested ($12 \times 10 \times 1 \mu\text{m}^3$; Figure S6-a), the system did not perform as desired (Figure S6-b–d). Cells within populations became desynchronised, and external signals were no longer strong enough to effectively propagate between populations.

Clearly, when directly adapted to take into account spatial dynamics in the location of bacterial populations, as well as diffusive signalling, the DDE model no longer predicts behaviour consistent with the observed experimental results. There are some shortcomings regarding the model’s parameters when spatial features are taken into account; this may put into question measurements taken from cell populations in order to identify models/parameters. For a given model, its parameters are often valid only in a certain context, or range of contexts. It is interesting that the DDE model does take into account the main dynamical features of the system as experimentally validated, in (S9); the spatially extended model requires adaptation in order to function as desired. In the case of the original DDE model, many model parameters were chosen from a large set of Monte-Carlo simulation generated distributions, in order to generate the desired behaviour (oscillations in the consortium). Mathematically speaking, there are a number parameter combinations that would satisfy this criterion as the study in (S9) does indeed show. However, not all of the parameters that are valid for the original DDE system are valid in the spatially extended system.

We found that in a more experimentally realistic scenario with both populations uniformly intermixed, the ‘best-case’ where signalling is concerned since the average inter-population distance between cells of the two types is minimised, the system performed as expected (Figure S8). Here the diffusive signalling between cells was most efficient and resulted in both a rapid and strong response across the population (consistent with the DDE model which does in fact assume the existence of such a ‘well-mixed’ population), and synchronisation

Table S2: Modified model parameters for the case study, used in delay equations adapted from (S9) coupled to a spatial chemical diffusion model.

Description	Parameter	Original value	Optimised value
Cell wall diffusivity of H	D_H	3 min^{-1}	6 min^{-1}
Cell wall diffusivity of I	D_I	2.1 min^{-1}	21 min^{-1}
Synthesis rate of H	ϕ_H	16 min^{-1}	8 min^{-1}
Synthesis rate of I	ϕ_I	2 min^{-1}	4 min^{-1}
External diffusion of inducers(S16)	D_{ext}	$800 \mu\text{m}^2\text{sec}^{-1}$	–
External degradation of inducers	μ_e	0.1 min^{-1}	0
Leak rate at open boundary	μ_{leak}	$800 \mu\text{m}^2\text{sec}^{-1}$	0.1 (original μ_e)

within cell populations (Figure S8-b).

In order to mitigate the significant effects of cell separation that were present in our worst-case scenario, and that would occur in any realistic situation where cells grow and cluster together, we optimised the parameters chiefly responsible for inter-cell signalling in the model: D_H , D_I , ϕ_H , ϕ_I (Figure S4, Table S2). We performed a wide-range perturbation over these parameters, consisting of 256 simulations of all combinations of 4 perturbations on each parameter. The best result was then refined within a smaller range of perturbations on each parameter resulting in the values indicated in Table S2. In this case, the cell wall diffusivity of both H and I were increased, meaning that cells were more efficiently able to sequester the lower concentrations of signalling molecules present in the spatially extended scenario. Meanwhile the synthesis rate of H was decreased, reducing the positive feedback strength within the Activator cells’ population, and the synthesis rate of I was increased strengthening the Repressor cells’ negative feedback effect that is necessary for the generation of robust population-wide oscillations. We were still unable to force the whole population of Activator cells to synchronise through this approach (Figure S4), however the average performance of the model was noticeably improved compared to the original parameters (Figure S6-c).

Furthermore, the optimised parameters did change the mean behaviour of the two cellular populations (see Figure S8) when simulations were run in a ‘well-mixed’ scenario where agents belonging to the two different populations are uniformly intermixed. Compared to

the original parameters, the strength of the Repressor cells’ output is approximately doubled, the strength of the Activator cells’ output is halved, and the overall period of oscillations is lengthened on average from 3 hours to approximately 4 hours. However otherwise the behaviour of the system remained qualitatively the same as previously.

Finally, we determined that it was indeed necessary to use the modified parameters in a full growth scenario, under the most realistic experimental conditions. Cells of both populations were initialised at random positions throughout a $100 \times 85 \times 1 \mu\text{m}^3$ microchemostat. Growth and division were enabled for all cells, and boundary conditions were set such that the leak rate was equal to μ_e in the original model. With the original model’s parameters from (S9), the system failed to either fully synchronise or to oscillate reliably (Figure S7). In contrast, using the modified signalling parameters the system behaved comparably to the in-vivo experiments presented in (S9) (Figure 1-c, and Movie S1), even when cells began to cluster together and mixing was no longer optimal. This can be explained by noting that the model in (S9) is simpler than the one adopted here as it does not explicitly take into account spatial characteristics of the system instead assuming (as in our ‘best-case’ scenario) that the two populations of cells are evenly distributed spatially and well mixed with respect to each other.

3.2.1 Note on selection of single cells

The single-cell time series shown in Figure 1-c(iii) and Figure S7-b) were computed as follows. All cells in the simulation were treated as individuals; mother-daughter cell lines were not explicitly tracked, however the age of each individual cell (simulation time since birth) was stored. Cells aged continuously through the simulation until the point at which they left the simulation domain, the time of which was effectively their time of death. On completion of the simulation, all individual cells were sorted by their total lifetime, and the 50 longest lived cells were selected. These 50 cells were then sorted by their birth time, and their time series were plotted as a heatmap in the aforementioned Figures.

3.2.2 Computational resources

All simulations in the case study were performed either on a workstation with two Intel® Xeon® E5-2630 v3 CPUs and 64Gb of RAM, or on an equivalently-specified node of the University of Bristol HPC facility ‘BlueCrystal’. In general, simulations were run on a single core; thus, where stochastic effects were present in the model multiple simulations could be run in parallel in a Monte-Carlo approach.

3.3 Implications for microfluidic chemostats

The design of microfluidic chambers is crucial for the success of in-vivo experiments, however the choice of an ‘optimal’ design often relies on a trial-and-error approach using physical devices, therefore resulting in a necessarily small exploration of the possible design space. For a growing population of cells of a single species, the effects of chamber geometry on growth and alignment are known (S2, S5). However, to date, few experiments have been undertaken to describe the effects of chamber geometry on engineered GRNs, and certainly the behaviour of multiple populations growing together in microfluidic devices has not been characterised.

It is relatively easy to obtain a stable population of a single engineered species, for example, using a confined rectangular chamber with a flow along one or more sides (S8). While this is adequate for investigating single-population quorum effects, in the case of consortia consisting of multiple interacting engineered species it is desirable to have a predictable, or controllable, ratio of the populations; this is not guaranteed with traditional microfluidic chemostat designs. The design studied here, while employed successfully in the experimental scenario of (S9), did not guarantee long-term stability of both populations especially when the dimensions of the microchemostat were reduced. Specifically, in our case study, 6 of 8 simulations undertaken in the $50 \times 42 \times 1 \mu\text{m}^3$ chamber lost one of the two populations, and 4 of 9 simulations undertaken in the $100 \times 85 \times 1 \mu\text{m}^3$ lost one population after 8 to 16 hours of experimental time had elapsed. This is clearly inadequate for performing experiments

that require observation of long-term dynamics.

Instead a chamber that is open on two opposite sides such as that employed *in-vivo* in (S10) for a single population, investigated *in-silico* with multiple populations in (S14), can guarantee stable growth of multiple different cellular populations. However, with both opposite edges of the chamber open to an external flow, the chemical quorum effect within the chamber may be weakened.

Furthermore, the effective total rate of signal degradation arises from the combined effect of the diffusion rate (D_{ext}) away from the neighbourhood of a bacterium, the local degradation rate μ_e , and the effective rate of loss at the chamber’s open boundaries. Specifically, as the rate of diffusion out of the chamber increases, the effective ‘degradation’ of signal increases. This results in a communication failure between the two consortia (see Figure S5); the range of viable diffusion-related loss rates (corresponding in reality to a range of external flow speeds) is relatively narrow.

References

- (S1) Gorochofski, T. E., Matyjaszkiewicz, A., Todd, T., Oak, N., Kowalska, K., Reid, S., Tsaneva-Atanasova, K. T., Savery, N. J., Grierson, C. S., and di Bernardo, M. (2012) BSim: an agent-based tool for modeling bacterial populations in systems and synthetic biology. *PloS one* 7, e42790–e42790.
- (S2) Cho, H., Jönsson, H., Campbell, K., Melke, P., Williams, J. W., Jedynek, B., Stevens, A. M., Groisman, A., and Levchenko, A. (2007) Self-organization in high-density bacterial colonies: efficient crowd control. *PLoS Biol.* 5, e302.
- (S3) Mather, W., Mondragón-Palomino, O., Danino, T., Hasty, J., and Tsimring, L. S. (2010) Streaming instability in growing cell populations. *Phys. Rev. Lett.* 104, 208101.
- (S4) Storck, T., Picioreanu, C., Viridis, B., and Batstone, D. J. (2014) Variable cell mor-

- phology approach for individual-based modeling of microbial communities. *Biophys. J.* *106*, 2037–48.
- (S5) Volfson, D., Cookson, S., Hasty, J., and Tsimring, L. S. (2008) Biomechanical ordering of dense cell populations. *Proc. Natl. Acad. Sci. U. S. A.* *105*, 15346–51.
- (S6) Jönsson, H., and Levchenko, A. (2005) An Explicit Spatial Model of Yeast Microcolony Growth. *Multiscale Model. Simul.* *3*, 346–361.
- (S7) Landau, L. D., Pitaevskii, L. P., Kosevich, A. M., and Lifshitz, E. *Theory of elasticity*; Butterworth-Heinemann, 1986; p 187.
- (S8) Danino, T., Mondragón-Palomino, O., Tsimring, L., and Hasty, J. (2010) A synchronized quorum of genetic clocks. *Nature* *463*, 326–30.
- (S9) Chen, Y., Kim, J. K., Hirning, A. J., Josi, K., and Bennett, M. R. (2015) Emergent genetic oscillations in a synthetic microbial consortium. *Science* *349*, 986–989.
- (S10) Mondragón-Palomino, O., Danino, T., Selimkhanov, J., Tsimring, L., and Hasty, J. (2011) Entrainment of a population of synthetic genetic oscillators. *Science (New York, N.Y.)* *333*, 1315–9.
- (S11) Akenine-Moller, T., and Haines, E. *Real-Time Rendering*, 2nd ed.; A. K. Peters, Ltd.: Natick, MA, USA, 2002.
- (S12) de Berg, M., Cheong, O., van Kreveld, M., and Overmars, M. *Computational Geometry: Algorithms and Applications*, 3rd ed.; Springer-Verlag TELOS: Santa Clara, CA, USA, 2008.
- (S13) Cantone, I., Marucci, L., Iorio, F., Ricci, M. A., Belcastro, V., Bansal, M., Santini, S., di Bernardo, M., di Bernardo, D., and Cosma, M. P. (2009) A Yeast Synthetic Network for In Vivo Assessment of Reverse-Engineering and Modeling Approaches. *Cell* *137*, 172–181.

- (S14) Fiore, G., Matyjaszkiewicz, A., Annunziata, F., Grierson, C., Saverly, N. J., Marucci, L., and di Bernardo, M. (2017) In-Silico Analysis and Implementation of a Multicellular Feedback Control Strategy in a Synthetic Bacterial Consortium. *ACS Synth. Biol.* 6, 507–517, PMID: 27997140.
- (S15) Balagaddé, F. K., Song, H., Ozaki, J., Collins, C. H., Barnet, M., Arnold, F. H., Quake, S. R., and You, L. (2008) A synthetic Escherichia coli predator-prey ecosystem. *Mol. Syst. Biol.* 4, 187.
- (S16) Mina, P., di Bernardo, M., Saverly, N. J., and Tsaneva-Atanasova, K. (2013) Modelling emergence of oscillations in communicating bacteria: a structured approach from one to many cells. *J. R. Soc., Interface* 10, 20120612.
- (S17) Jang, S. S., Oishi, K. T., Egbert, R. G., and Klavins, E. (2012) Specification and simulation of synthetic multicelled behaviors. *ACS Synth. Biol.* 1, 365–374.

4 SI Figures and Movies

4.1 Supplementary Figures

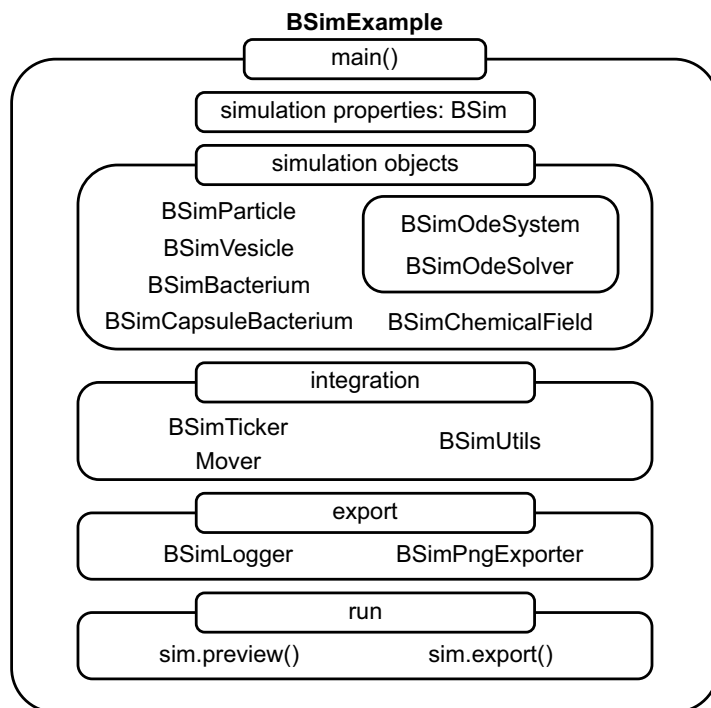


Figure S1: An outline of the hierarchical and sequential structure of a BSim simulation’s definition, referred to here as the ‘BSimExample’. The BSimExample consists of a ‘main()’ method, which facilitates entry into the program and allows it to be externally executed in order to run the simulation. Simulation properties are first defined in the core BSim object. One can then define a desired combination of simulation objects that they wish to have included in the experiment, including cells, ODE/DDE systems, and chemical fields (which permit signalling through aggregate diffusion); these can be coupled together in some ways, e.g., a BSimBacterium may contain a BSimOdeSystem and may be coupled to a BSimChemicalField. Integration through time is defined through a BSimTicker. Additionally, one may specify a ‘Mover’ that integrates the positions of capsular bacteria by computing their physical interactions with each other and the environment. Finally one can define a set of exporters, to record data as the simulation runs, and must subsequently run the simulation using a preview (rendered to screen) or export mode (where data is recorded using the exporters defined above).

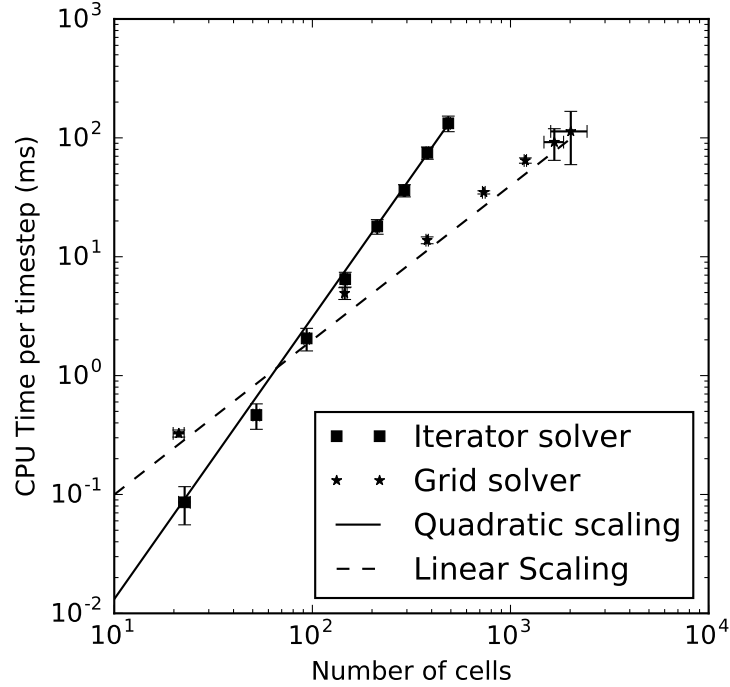


Figure S2: Simulation scaling and performance. Simulations were undertaken in a microfluidic chemostat geometry, of the same design as in our case study (closed on all sides apart from one; see Figure S3). The chemostat was initialised with a population of 10 bacteria; these were allowed to grow and divide, reaching a dynamic equilibrium, at which point the simulation was continued for a total of 100 further timesteps. The chemostat dimensions were varied between $10 \times 10 \times 1 \mu\text{m}^3$ and $100 \times 100 \times 1 \mu\text{m}^3$ in order to obtain representative timing measures for a variety of simulation sizes. The number of cells and the time required to perform a full collision resolution and position constraint correction were recorded at each timestep. The mean population, and mean time (ms) required to complete collision iterations, for the final 50 timesteps of each simulation are plotted for the iterative solver (squares) and for the grid solver (stars); x and y error bars indicate SD for population size and CPU time respectively over the 50 timesteps plotted. The solid line indicates quadratic scaling of CPU time per simulation timestep with respect to number of bacteria, and the dashed line indicates (improved) linear scaling of the grid solver.

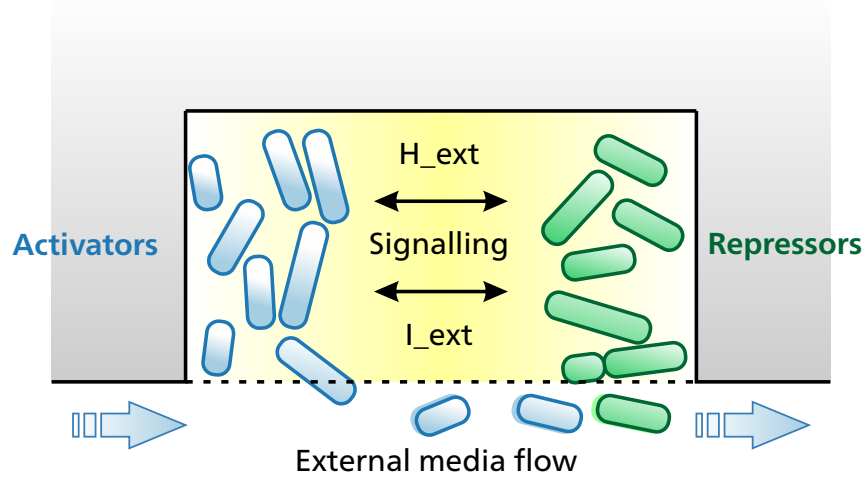


Figure S3: Case study: model implementation. The original DDE system of 16 equations was split across two discrete cell populations (Activator cells: blue, Repressor cells: green). These were coupled via external diffusion in a 3D chemical field modelled by discretised diffusion equations. The cells were embedded within a virtual microfluidic chemostat with rectangular geometry, with dimensions ranging between $12 \times 10 \times 1 \mu\text{m}^3$ (the smallest size investigated) and $100 \times 80 \times 1 \mu\text{m}^3$ (the largest, corresponding to the chamber used in (S8) for example); simulations of the different sized chambers with fixed populations are shown in Figure S6-a–d. All boundaries were considered fixed except for the lower boundary which was open to both diffusion and the physical passage of cells, allowing for a flux of cells to occur into the external media flow as the population grew.

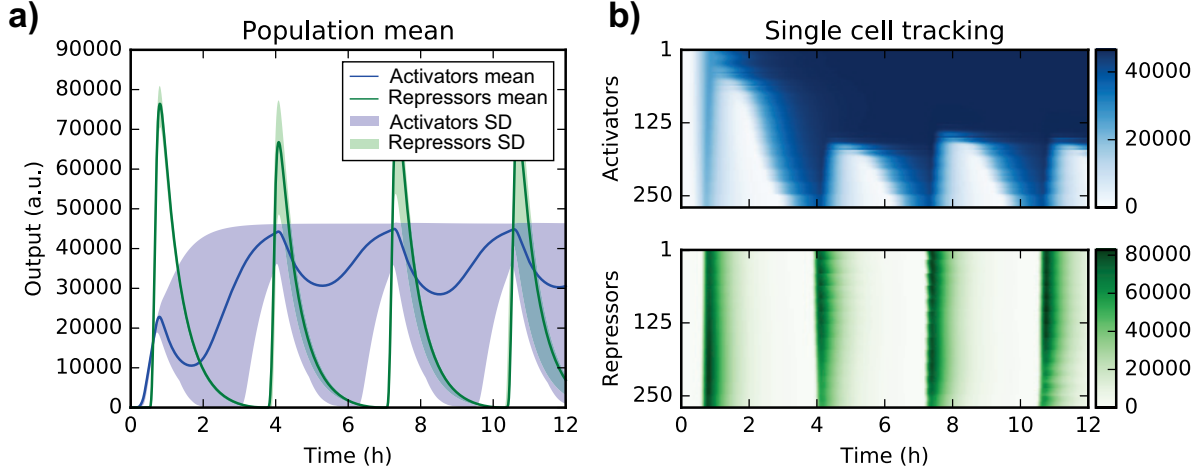


Figure S4: Parameter modifications relating to generation and diffusion of I . We ran 256 simulations ranging over combined perturbations in D_H , D_I , ϕ_H , ϕ_I , the parameters related most closely to intercellular signalling. This wide-range characterisation was then refined resulting in the optimised parameters indicated in Table S2. Here, we plot the simulation output for the optimised signalling parameter set. Simulations were run with populations initialised in two separate uniform-density blocks (as in Figure S6) in the half-sized $50 \times 42 \times 1 \mu\text{m}^3$ microfluidic chemostat, corresponding to a worst-case experimental scenario. Growth and division were not included in the model; a fixed number of 525 cells were simulated, with Activator and Repressor cells' populations each comprising exactly half of this total. a) The mean of each population's output is plotted, for Activator cells (blue) and Repressor cells (green). Solid lines indicate the mean population output for each species; the filled regions indicate the range (min-max) of each population's output. b) Single-cell output amplitudes for the entire population. The amplitudes of fluorescence outputs measured from Activator cells (blue) and Repressor cells (green) are indicated; time series are plotted for all individual cells (rows), with simulation time increasing left-to-right.

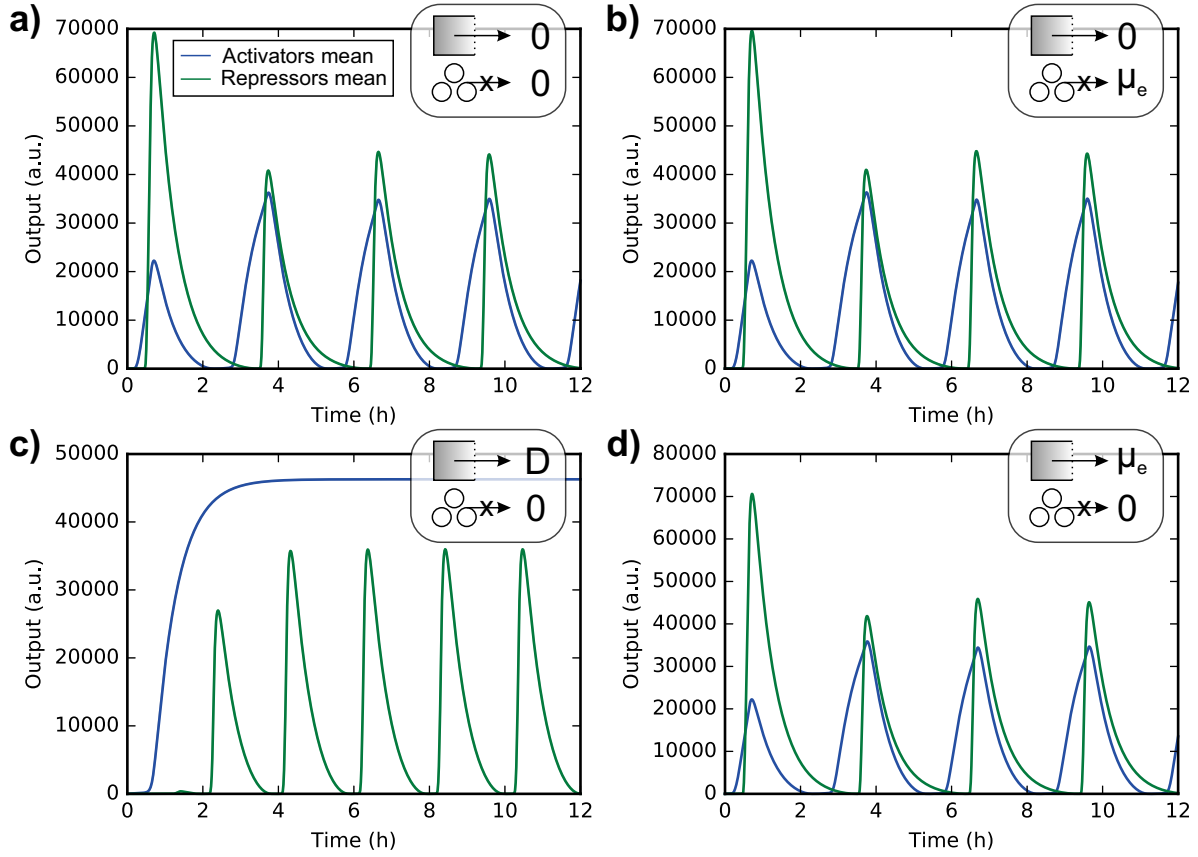


Figure S5: Two-cell model simulations. The degradation of external signalling chemicals, and the open boundary condition (Figure S3), were varied to test the conditions of our *BSim 2.0* case study implementation. A single Activator cell and single Repressor cell were placed, at a uniform distance of $5\mu\text{m}$ from one another, in a $12 \times 10 \times 1\mu\text{m}^3$ chamber. The cells were not permitted to move or grow throughout the duration of the simulation. a) No flux through the open boundary; and no spatial degradation term. b) No flux through the open boundary; spatial degradation set to a uniform value of $\mu_e = 0.1$ as in the original DDE model shown in (S9). c) Open boundary flux set equal to the diffusion coefficient of each signalling chemical, D , equivalent to a real experimental scenario in which signalling molecule transport at the chamber boundary is diffusion-limited; no separate spatial degradation. d) Open boundary flux set to $\mu_e = 0.1$; no separate spatial degradation.

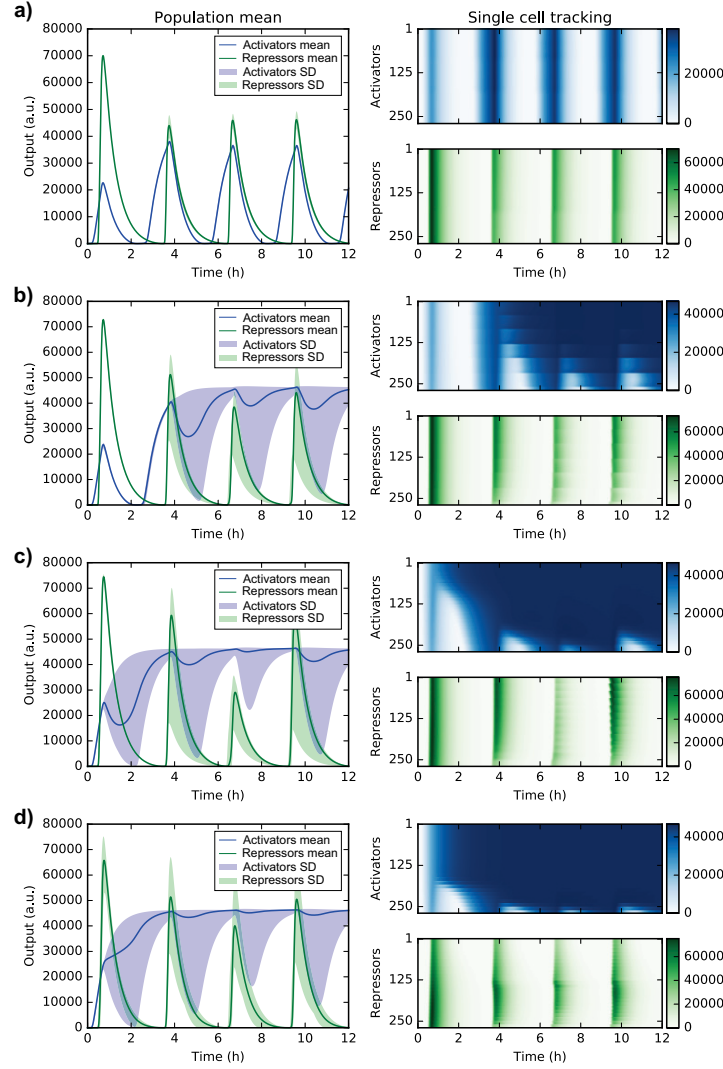


Figure S6: Model failure as domain size and average cell-cell distance are increased. The size of the microfluidic chemostat was varied as follows: a) $12 \times 10 \times 1 \mu\text{m}^3$; b) $25 \times 20 \times 1 \mu\text{m}^3$; c) $50 \times 42 \times 1 \mu\text{m}^3$; d) $100 \times 85 \times 1 \mu\text{m}^3$. Cells were initialised with uniform density in two separate halves of the domain (Activator cells in the left half, Repressor cells in the right half). Cell density was chosen such that the chamber was completely filled at each size: a) 30 cells; b) 130 cells; c) 525 cells; d) 2125 cells. Growth and division were not included in the model. For each chamber size, the mean of the population output is plotted, for Activator cells (blue) and Repressor cells (green). Solid lines indicate the mean population output for each species; the filled regions indicate the range (min–max) of each population’s output. In each case, panels on the right show the single-cell output amplitudes for the entire population. The amplitudes of fluorescence outputs measured from Activator cells (blue) and Repressor cells (green) are indicated; time series are plotted for all individual cells (rows), with simulation time increasing left-to-right.

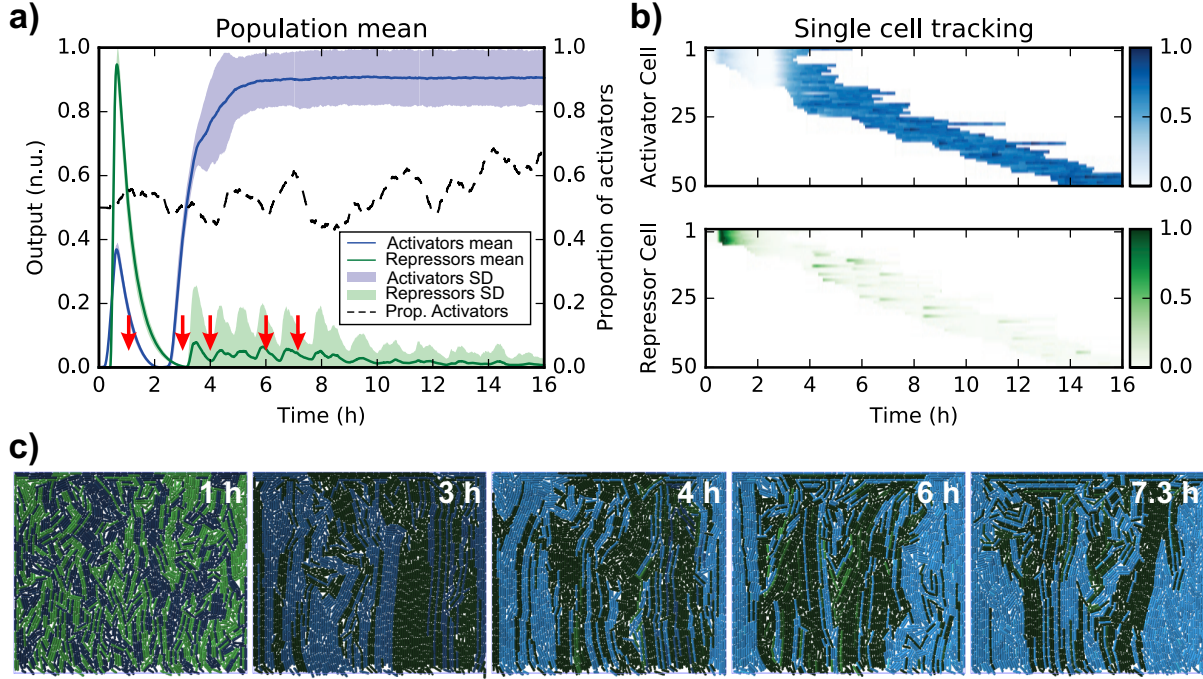


Figure S7: Results of our spatially extended case study, with original cell-cell signalling parameters. a) Simulation with realistic cell morphology, growth and division with cells initialised at randomly chosen positions, in a full-sized $100 \times 85 \times 1 \mu\text{m}^3$ rectangular microfluidic chemostat. Mean population output (solid lines) is plotted, for Activator cells (blue) and Repressor cells (green); filled regions indicate mean \pm SD. Black dashed line indicates the proportion of activator cells present in the chemostat over time. b) Single-cell output is plotted from the 50 longest-lived cells in the simulation (see section 3.2.1); the amplitudes of fluorescence outputs measured from Activator cells (blue) and Repressor cells (green) are indicated; time series are plotted for 50 individual cells (rows), with simulation time increasing left-to-right. c) Simulation snapshots rendered at points indicated by red arrows in (i). Individual cells are indicated by capsules, coloured blue (Activator cells) and green (Repressor cells), with the intensity of each colour corresponding directly to the level of output fluorescence. Simulations were initialised with 500 cells of each type; the filled chamber (snapshots) contains on average 2150 cells when full.

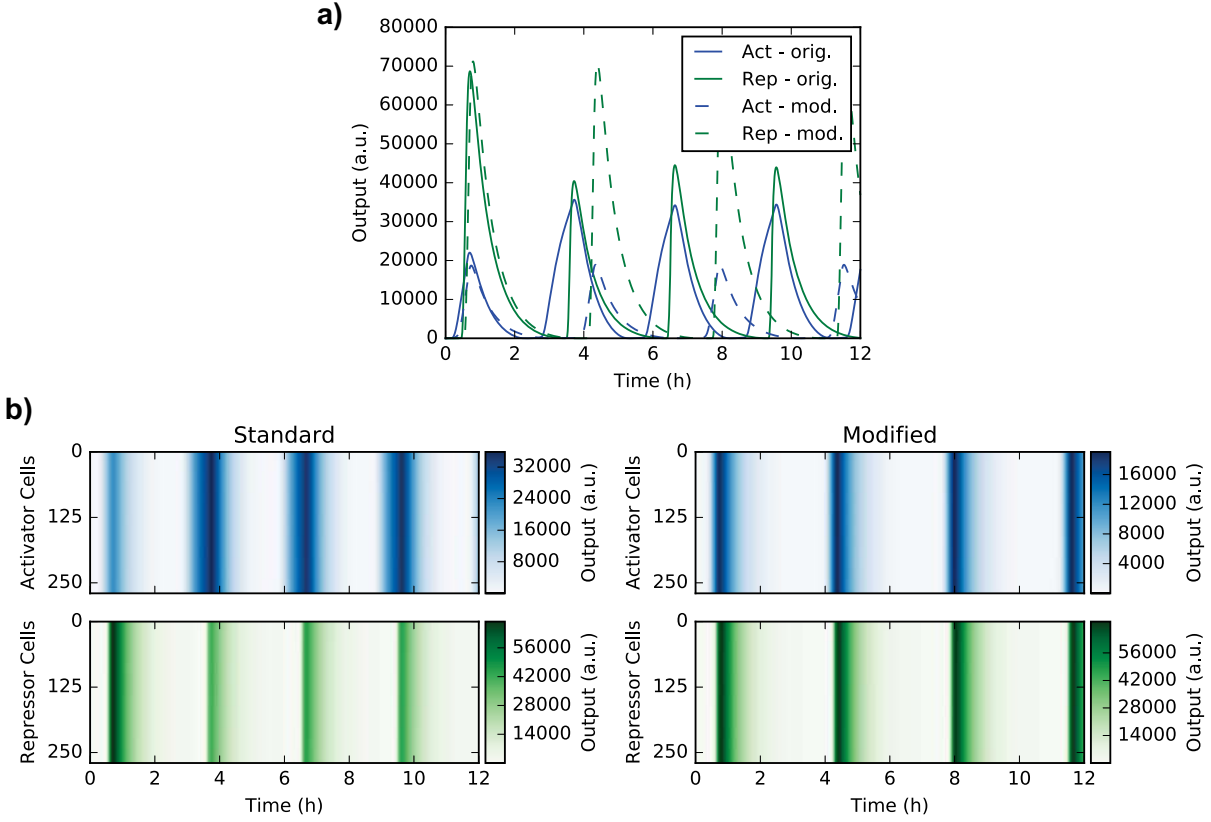


Figure S8: A ‘well-mixed’ population scenario guarantees good model performance that is equivalent to the continuum DDE model. The two cell populations were simulated at fixed positions uniformly mixed and distributed throughout the half-sized $50 \times 42 \times 1 \mu\text{m}^3$ microfluidic chemostat; a fixed number of 525 cells were simulated, with Activator and Repressor cells’ populations each comprising exactly half of this total. a) The mean of the population output is plotted, for Activator cells (blue) and Repressor cells (green). Solid lines indicate the mean population output for a simulation with the original model’s signalling parameters; dashed lines indicate the mean output when optimised signalling parameters were used. b) Single-cell output amplitudes for the original (left) and optimised (right) parameters. The amplitudes of fluorescence outputs measured from Activator cells (blue) and Repressor cells (green) are indicated; time series are plotted for 260 individual cells (rows), with simulation time increasing left-to-right.

4.2 Supplementary Movies

Supplementary Movie S1: Agent-based simulation of consortium oscillator case study, corresponding to data and snapshots shown in Figure 1-c. The left panel shows a 3D rendering of the BSim simulation: Activator cells are depicted as blue capsules, and Repressor cells are colored green. The color intensity is proportional to the level of measurable output of the individual Activator cells (mature CFP; M_a in the original DDE model) and Repressor cells (mature YFP; M_r in the original DDE model) at the given time instant. The simulation was performed in a $100 \times 85 \times 1 \mu\text{m}^3$ chamber (boundary indicated by purple box outline). Cells were initialized at uniformly distributed positions throughout the chamber, with a uniformly mixed distribution of both populations consisting of 500 rod-shaped Activator cells and 500 Repressor cells. Growth and cell division were included in the model. The average total number of cells in the simulation once the chamber was full (after 1 hour) was approximately 2150. All cells' parameters were uniform in this simulation. The three panels on the right hand side indicate, from top to bottom: the distribution of outputs (Activator cells, blue; Repressor cells, green) as a histogram at the current time instant; the mean output of the Activator cell population (blue line) and of the Repressor cell population (green line) over time; the number of Activator cells (blue line) and Repressor cells (green line) active in the simulation over time. The current time instant of the simulation is indicated by filled circles in each time series.